Effect of inclusion of MOF-polymer composite onto a carbon foam material for hydrogen storage application

Lerato Y. Molefe[1,2], Nicholas M. Musyoka[1,2]*, Jianwei Ren[1], Henrietta W. Langmi[1,3], Mkhulu Mathe[1], Patrick G. Ndungu[2]

[1]HySA Infrastructure Centre of Competence, Centre for Nanostructures and Advanced Materials (CeNAM), Chemicals cluster, Council for Scientific and Industrial Research (CSIR), Meiring Naude Road, Brummeria, Pretoria 0001, South Africa.

[2]Energy Sensors and Multifunctional Nanomaterials Research Group, Department of Chemical Sciences, University of Johannesburg, Doornfontein Campus, South Africa.

[3]Department of Chemistry, University of Pretoria, Pretoria, South Africa.

**Corresponding author: nmusyoka@csir.co.za, Tel: +27 12 841 4806 (N.Musyoka)*

Abstract

Despite the extensive studies done on the remarkable characteristics of metal-organic frameworks (MOFs) for gas storage applications, several issues still preclude their widespread commercial lightweight applications. In most cases, MOF materials are produced in powdery form and often require shaping to attain application-specific properties. Fabrication of MOF-polymer composites is considered an attractive approach for shaping MOF powders. In most cases, the final hybrid material retains the intrinsic adsorbing properties of the pristine MOF coupled with other interesting synergistic features which are sometimes superior to their pristine counterparts. In this regard, the use of porous polymers of intrinsic microporosity (such as PIM-1) has proved to be of interest. However, most of these polymers lack some other important properties such as conductivity, which is of paramount importance in a hydrogen storage system. It is on this basis that our study aimed at direct anchoring of a PIM-1/MOF viscous solution onto a carbon foam (CF) substrate. The effects of PIM-1/UiO-66(Zr) inclusion into CF to the resulting thermal properties (thermal conductivity, thermal diffusivity and volumetric heat capacity) as well as hydrogen uptake capacity was investigated. Contrary to our expectations, the incorporation of PIM-1/UiO-66(Zr) into CF only offered better handling but did not lead to the enhancement of thermal conductivity.

Keywords: Carbon foam, hydrogen storage, metal organic frameworks, polymers of intrinsic microporosity.

1. Introduction

The harmful gaseous and particulate emissions from the combustion of fossil fuels has led to global warming and poor air quality, which have detrimental effects to the environment and human health. Therefore, to address this challenge, there is a need to develop and embrace alternative low emission, cost-effective and efficient energy technologies. Recently, there has been a growing interest in the use of hydrogen (H_2) as the future energy carrier. Hydrogen is considered a viable alternative fuel due to its abundant sources and clean combustion in which only water is released as a by-product **[1]**. However, H_2 gas has very low volumetric energy density, making compression at very high pressures (~ 700 bar) difficult. In this regard, on-board storage of hydrogen gas presents the main obstacle for applications of H_2 fuel in automobiles. Research in this area is mainly driven by the proposed criteria set by the United States Department of Energy (U.S DOE) for an on-board H_2 storage system for the year 2020. In this case, the required volumetric and gravimetric storage capacities are set at 0.030 kg H_2/L and 4.5 wt.% respectively **[2]** Unfortunately, at the moment, none of the current H_2 storage technologies have met the aforementioned U.S DOE specifications.

Nanoporous sorbent materials such as metal-organic frameworks (MOFs), zeolites, carbon and porous polymers play a significant role in industrial applications such as catalysis, gas storage and separation membranes **[3-6]**. Amongst these materials, MOFs exhibit attractive properties which are excellent for their use in H_2 storage. For instance, MOFs possessing surface areas exceeding 6000 m^2g^{-1} such that MOF-210 **[7]** and NU-100 **[8]** are excellent for H_2 storage. However, since MOFs crystals are obtained as fine powders, they suffer from poor processability and low thermal conductivity. To this effect, various types of carbon-based MOF composites that include materials such as graphene, carbon nanotubes, and templated carbons have been investigated as H_2 storage materials owing to their electrical and thermal conductivity, chemical and mechanical stability properties **[5-8]**. However, the issue of structural integrity remains a challenge **[13-15]**.

Several thermoplastic additives such as polystyrene, acrylonitrile butadiene styrene, polymethyl methacrylate have been used as binders for MOF powders **[16]**. However, they often result in pore-blocking effects which lead to reduced MOF surface areas. In this regard, the use of a polymer of intrinsic microporosity (PIM-1) which has surface areas of ~700 m^2g^{-1}, and is processable, can be recommended. In our previous study, we reported on the use of PIM-1, as a MIL-101(Cr) binder, which exhibited high surface area (2347 m^2g^{-1}) and H_2 uptake

(1.73 wt.%) at 77 K and 1 bar, thus showing great promise in H_2 storage **[17]**. To advance MOF shaping strategies, carbon foam (CF) which is a three-dimensional material consisting of interconnected macropores forming an open cell structure **[18],** can also be considered. Due to CF desirable properties such as its 3D hierarchical porous structure, lightweight and other features mentioned above for carbons, it has found applications in catalysis, carbon monoxide and carbon dioxide gas adsorption and thermal storage **[19-21]**. In this regard, CF can also be recommended for use as support material for immobilising MOFs.

In a previous study by Pinto and co-workers **[22]**, attempts were made to support Universitetet i Oslo zirconium-carboxylate (UiO-66(Zr)) MOF crystals onto polyurethane foam (PUF) but this did not completely solve the conductivity issue of MOFs because polyurethane is an insulator. Moreover, their *in-situ* approach resulted in slightly altered PUF composites structures. Nonetheless, the composites only retained about 55–60 % of the initial surface area and microporous volume. While the direct growth of MOFs onto porous templates is commonly employed, Ren and co-workers **[23]** applied an *ex-situ* spray-coating technique to generate multi-layers of MIL-101(Cr) onto a macroporous nickel foam. The resulting composites had a maximum loading of 81 wt% of MIL-101(Cr) and found to exhibit a H_2 uptake capacity of 1.5 wt.%, at 77 K and 1 bar. This study demonstrated a facile method for processing MOF powders for practical applications in H_2 storage systems, but the thermal conductivity studies were not reported. In this study, we explore the immobilisation of PIM-1/UiO-66(Zr) onto a CF through *ex-situ* inclusion approach. The chemically stable UiO-66 MOF was chosen because it is one of the most studied MOFs, and the structure is well-known. Furthermore, it has a high surface area, is robust, and its hydro-stability makes it a highly competitive MOF in hydrogen storage applications.

In this context, the effect of inclusion of polymer-based MOF composites into a CF foam to its physical properties and hydrogen storage capacity was investigated. The resulting hierarchical composite material possessed some synergistic properties brought about by the increased amount of micro-meso pores inside the macropores of CF.

2. Experimental Section

2.1.Materials and chemicals

Porous materials presented in this study were prepared using the following chemicals, and were used as-received without further purification: terephthalic acid (BDC, 98%, Sigma-Aldrich),

dimethylformamide (DMF, 99.8%, Sigma-Aldrich), formic acid (HCOOH, 99.5+%, Sigma-Aldrich), zirconium tetrachloride ($ZrCl_4$, 99.5+%, Sigma-Aldrich), ethanol (CH_3CH_2OH, 90%, Ace chemicals), potassium carbonate (K_2CO_3, 99+%, Sigma-Aldrich), 5,5',6,6'-tetrahydroxy-3,3,3',3'-tetramethyl-1,1'-spirobisindane (TTSBI, Sigma-Aldrich), tertrafluoroterephthalonitrile (TFTPN, 99%, Sigma-Aldrich), anhydrous chloroform ($CHCl_3$, 99.9+%, Sigma-Aldrich), methanol (CH_3OH, 99.9+%, Sigma-Aldrich), 1,1,2,2-tetrachloroethane ($CHCl_2CHCl_2$, 98.0+%, Sigma-Aldrich), de-ionized water and activated carbon-based foam (CF). Nitrogen (N_2) and Hydrogen (H_2) gases of ultra-high purity grade, purchased from Afrox Company in South Africa, were used for sample analyses.

2.2. PIM-1 synthesis

The synthesis of PIM-1 was carried out according to the method reported by Budd et al. **[24]**. Briefly, a mixture consisting of an equimolar composition of 5,5',6,6'-tetrahydroxy-3,3,3',3'-tetramethyl-1,1'-spirobisindane (5.11 g) and tertrafluoroterephthalonitrile (3.00 g) in the presence of anhydrous K_2CO_3 (16.59 g) catalyst was transferred into a 250 mL three-neck round-bottom flask. The mixture was then evacuated and back-filled with nitrogen gas, and anhydrous DMF (100 mL) was subsequently added. The resulting solution mixture was then heated under reflux conditions at 65 ºC, under N_2 gas and constant vigorous magnetic stirring for 72 h. The recovered yellow precipitate was cooled down to room temperature and added to 300 mL of water while stirring for an hour without heat. The resulting solid was vacuum filtered, dried at 80 ºC under vacuum and then dissolved in anhydrous chloroform before re-precipitation in methanol. The re-precipitation cycles were repeated for three times, and the final product collected by filtration was dried at 60 ºC for two days in a vacuum oven. The simplified synthesis method is also presented in **Fig.1**.

2.3.Synthesis of UiO-66(Zr)

UiO-66(Zr) MOF crystals were synthesised following an optimised solvothermal synthesis method reported elsewhere **[25]** but with some minor amendments. Briefly, the method involved the mixing of 1.06 g (4.54 mmol) of zirconium tetrachloride, 0.68 g (4.09 mmol) of terephthalic acid in 50 mL of DMF. The resulting solution was ultrasonicated for 30 minutes, and 17.2 mL (0.454 mol) of the formic acid modulator was subsequently added to the mixture. The resulting mixture was then transferred into a 250 mL round bottom flask that had been fitted with a reflux system, placed in a hot oil bath and then heated to 120 °C. The reaction mixture was kept at this temperature for 4 h, under static conditions. After the reaction, the

resulting white precipitate product was collected by centrifugation at 10000 rpm for 15 min. The resulting precipitate was further washed with ethanol at 60 °C under stirring for 3 h and subjected to another cycle of centrifugation to remove the unreacted BDC reagent. Finally, the MOF crystals were dried at 90 °C in a conventional drying oven for 12 hours. The schematic illustration of the synthesis procedure is also presented in **Fig.1** below.

2.4.Fabrication of carbon foam immobilised PIM-1/UiO-66(Zr) composite structure

Unlike in the context of PUF/UiO-66(Zr) study **[22]**, the carbon foam (CF) could not withstand the solvothermal conditions for UiO-66(Zr) synthesis due to the chemical instability of CF in acidic media at high temperatures. Additionally, when MOF powder was dusted onto the CF, it was found to be still loose and fell off easily from the foam. Therefore, the direct impregnation of the CF with PIM-1/UiO-66(Zr) solution mixture was found to be a viable route for retaining the structure of CF. The processability of PIM-1 made the binding and immobilisation of the MOF onto CF relatively easy. In this case, an impregnation method was employed. Firstly, small cubic-shaped pieces of CF substrate were prepared by washing and sonication in deionised water and then dried in a vacuum oven. These pieces were then immersed in a mixture of PIM-1/UiO-66(Zr) prepared using tetrachloroethane (TCE) solvent. The foam pieces were then left to soak in the mixture for 12 hours to ensure maximum infiltration of PIM-1/UiO-66(Zr) into the macro-pores of the CF. Subsequently; the CF/PIM-1/UiO-66(Zr) composite sample was heated on a heating plate at 150 °C, for 12 h, to evaporate the trapped TCE solvent.

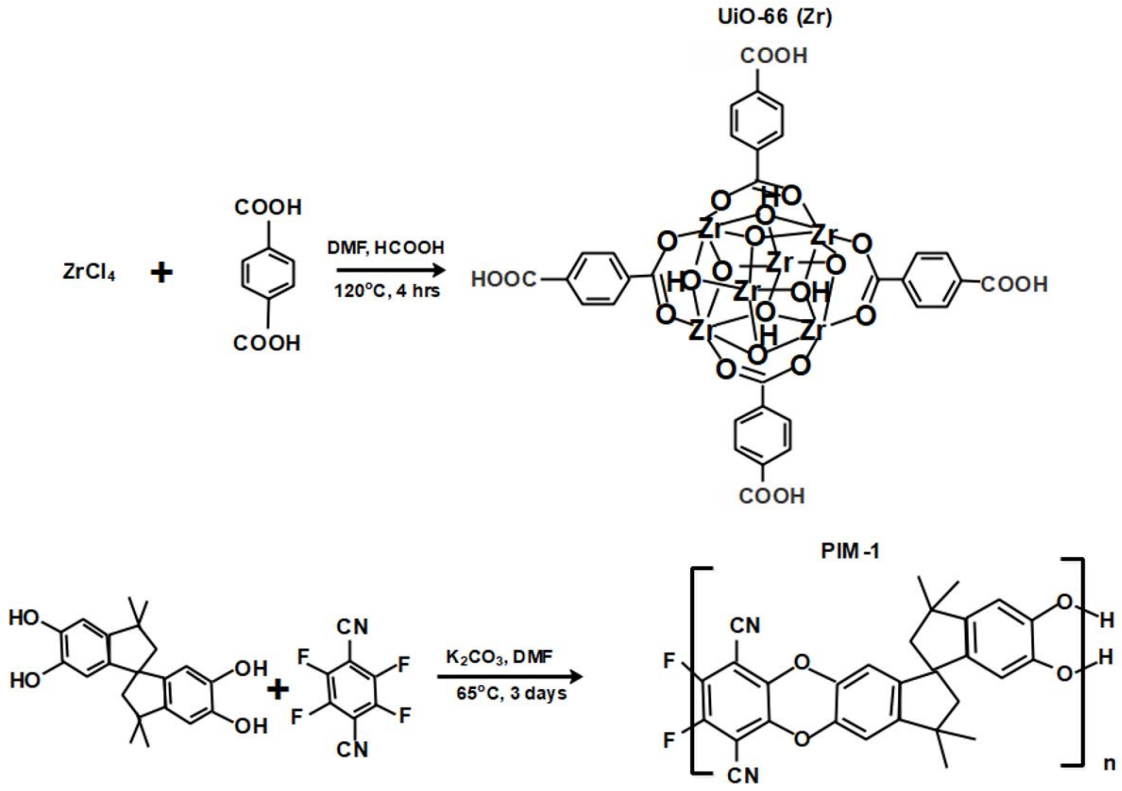

Fig.1 Schematic representation of the chemical reactions for the synthesis of the pristine UiO-66(Zr) MOF and PIM-1 materials

2.5.Sample characterisation

Powder X-ray diffraction (PXRD) patterns were obtained at room temperature using a PANalytical X'Pert Pro powder diffractometer, coupled to a Pixel detector with Cu-K_α radiation (0.154 nm) and scanning rate of 2^o min^{-1}. Carl Zeiss Auriga Cobra Focused ion beam scanning electron microscope (FIB-SEM) was used for morphological analysis of samples. The thermogravimetric analysis (TGA) curves were measured on a Mettler, Toledo, TGA/SDTA 851^e instrument, the samples were heated to ~1000 ºC with a heating rate of 10 ºC min^{-1}under air (60 ml min^{-1}) and nitrogen flow was maintained at 40 ml min^{-1} as balance gas. The thermal conductivity, thermal diffusivity and specific heat of the CF samples were measured using a Hot Disk TPS 500 thermal constant analyser (ThermTest Inc.) with the transient plane source method at room temperature (24 ºC). Measurements were carried out by sandwiching two flat pieces of samples with a Kapton disk sensor (3.2 mm) with a heating power of ~ 94.34 mW. Brunauer, Emmett and Teller (BET) surface areas and pore size distributions (PSDs) were determined from nitrogen (N_2) isotherms, which were obtained using a Micrometrics ASAP 2020 HD analyser 77 K. Before any gas adsorption experiment, the samples were outgassed in

the degassing port under vacuum (down to 10^{-7} bar) for at least 8 h at 200 ºC in order to remove any humidity and other physisorbed gases. Low-pressure hydrogen isotherms (up to 1 bar) were obtained using a Micrometrics ASAP 2020 HD analyser. All gas sorption experiments were performed at 77 K, using liquid nitrogen.

3. Results and Discussion

The comparative diffraction patterns of pristine materials and their corresponding composites are presented in **Fig.2a**. The crystalline structure of pristine UiO-66(Zr) was obtained, as confirmed by the presence of the two main characteristic diffraction peaks (2-theta = 7° and 9º) which are consistent with results reported in the literature **[26, 27]**. The two broad diffraction peaks centred at 2-theta = 20° and 2-theta = 43° which are characteristics for graphite corresponding to the (002) and (100) lattice planes respectively, were observed for the carbon-based CF **[28-31]**. This pattern indicates a predominantly amorphous structure. Similarly, the diffraction pattern of CF and PIM-1 presents amorphous characteristics (**Fig.2a**). The CF and PIM-1 structures were retained in diffractogram of the CF/PIM-1 composite. It can be easily seen that the diffractograms of CF/UiO-66(Zr) and CF/PIM-1/UiO-66(Zr) displayed a diffraction pattern similar to that of UiO-66(Zr), with a slight peak broadening effect coming from the presence of CF. This observation indicated successful immobilisation of the UiO-66(Zr) onto the CF as the UiO-66 (Zr) MOF crystalline structure was retained and no other new structure was formed.

The thermal degradation behaviour of the pristine materials (UiO-66 and PIM-1) and the CF/PIM-1/UiO-66(Zr) composite was studied using TGA and the thermograms are presented in **Fig.2b**. The TGA results of PIM-1 reveal two weight-loss steps, whereas UiO-66(Zr) and CF/PIM-1/UiO-66(Zr) exhibited three mass-loss levels. The first weight loss, which occurred below 150 °C for all samples, relates to dehydration and the loss of solvent molecules. The TGA profiles of UiO-66(Zr) and CF/PIM-1/UiO-66(Zr) showed a second thermal degradation step between 150 and 362 °C resulting from dehydroxylation of Zr_6 clusters and the decomposition of the BDC linker **[22, 32]**. Then the last thermal degradation step above 475-545 °C was attributed to the final decomposition of the MOF structure to ZrO_2 residue **[22, 33]**. Consequently, the PIM-1 was only stable up to 415 °C. On the other hand, the thermal degradation temperature of the CF/PIM-1/UiO-66(Zr) composite was found to be slightly higher (434 °C) than that of the pristine PIM-1, which indicates the contribution of high thermal stability of UiO-66 within the composite.

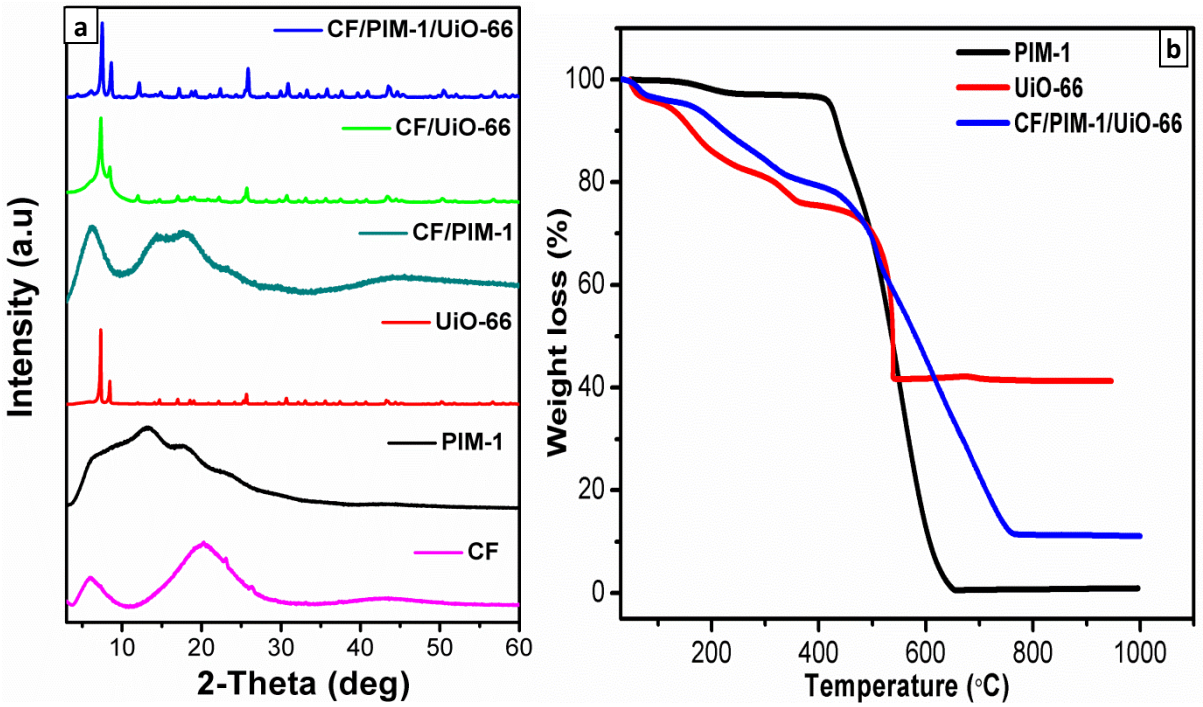

Fig.2 Stacked PXRD patterns (**a**) and TGA curves (**b**) of CF/UiO-66/PIM-1 based composites and their pristine counterparts

SEM image of pristine CF (**Fig.3a**) shows an open-cell/skeleton of highly interconnected large macropores surrounded by carbon walls throughout the structure. As reported in our previous studies [**17**], the PIM-1 sample exhibited rough morphological features due to the evaporation of the solvent during the vacuum drying process (**Fig.3b)**. In **Fig.3c**, the well-dispersed octahedral crystals of UiO-66(Zr) were observed, while the magnified image shown in **Fig.3d** clearly indicates that both the MOF crystals and polymer are anchored to the pore wall/boundary. The PIM-1 and UiO-66 crystals did not completely infiltrate through the open cell macropores of the foam as observed in **Fig.3e**. Thus, the octahedral shaped UiO-66(Zr) in PIM-1 matrix forming a sieve-in-a-cage morphology of PIM-1/UiO-66(Zr) was dominant and quite dense on the CF surface. Therefore, the SEM images indicated successful incorporation of UiO-66(Zr) crystals and PIM-1 onto the CF, which aligns with the PXRD and TGA findings.

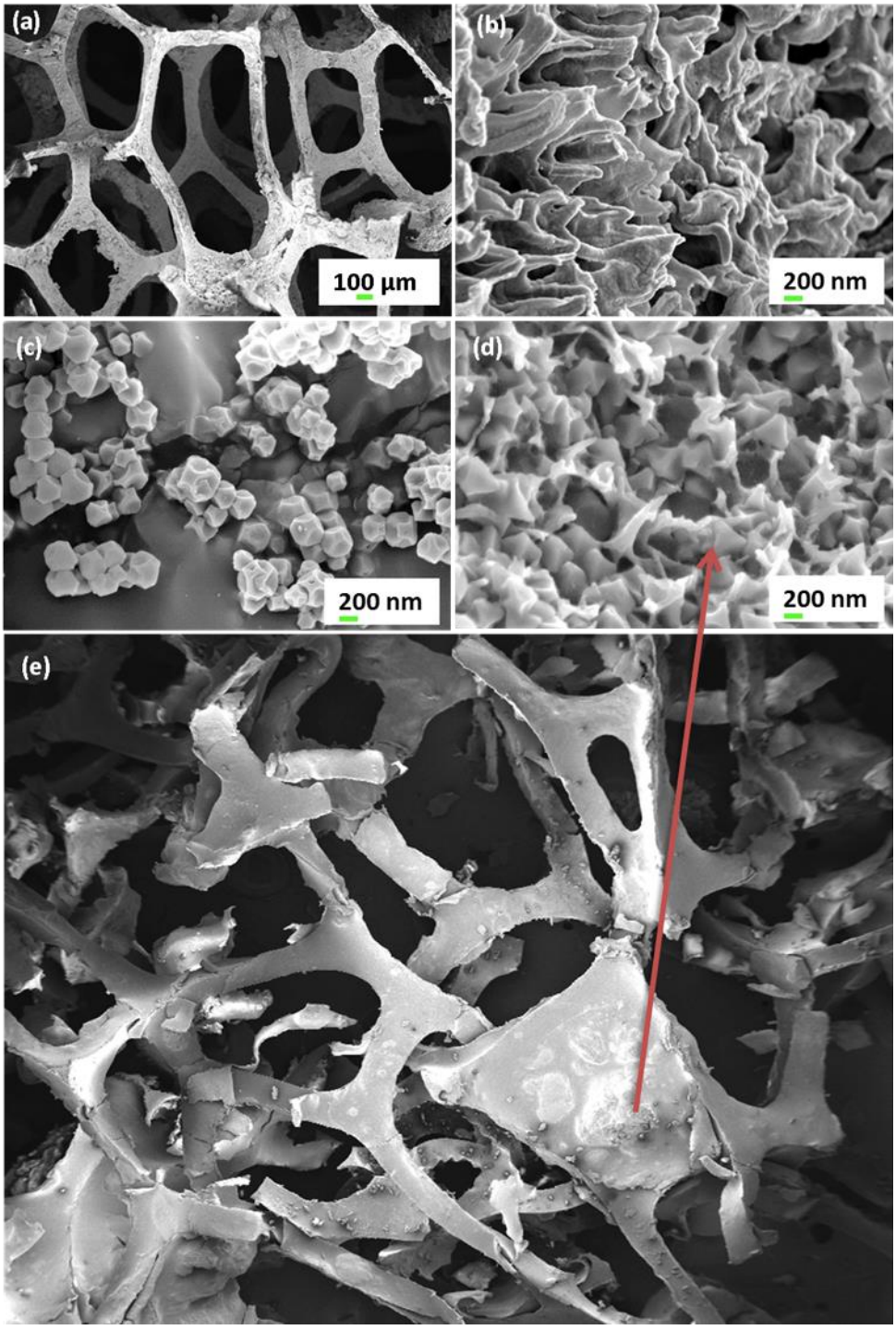

Fig.3 High resolution SEM images of carbon foam (CF) (**a**), PIM-1 (**b**), UiO-66 (**c**), CF/UiO-66/PIM-1 (**d-e**)

The sorption capabilities of the pristine and composite materials were confirmed by nitrogen adsorption at cryogenic temperature, from which the porosities and specific surface areas were also calculated (**Fig.4a**). The N_2 isotherms, at 77 K, for pristine UiO-66(Zr) exhibited a type I isotherm which is indicative of the microporous nature of the adsorbent (< 2 nm). On the other

hand, PIM-1 powder and CF/PIM-1/UiO-66(Zr) samples exhibited a type IV isotherm with almost similar hysteresis loops in which case the first part of the isotherm (at low P/Po axis) indicates a complete monolayer coverage on mesopores (< 50 nm) surfaces. For the pristine CF, a type V isotherm with a desorption curve having a type H1 hysteresis loop (IUPAC classification) was observed which suggested the presence of macropores (> 50 nm), which was confirmed with the SEM observations (**Fig.3a**) **[3]**. This observation is ordinarily common for water adsorption on activated carbon, which therefore makes sense since the analysed sample is an activated carbon-based foam **[34]**. The PSD curve (**Fig.4b**) of the CF/PIM-1/UiO-66 showed a relatively narrow multimodal pore size distribution centred at 1.9 nm (from UiO-66), 2.5-3.3 nm (of PIM-1) and a series of peaks at 4.4–9.9 nm (matching with CF peaks). The PSD, confirmed the earlier observations of the SEM and XRD analysis further indicating the co-existence of all the components present in the composite and a hierarchical characteristic as anticipated.

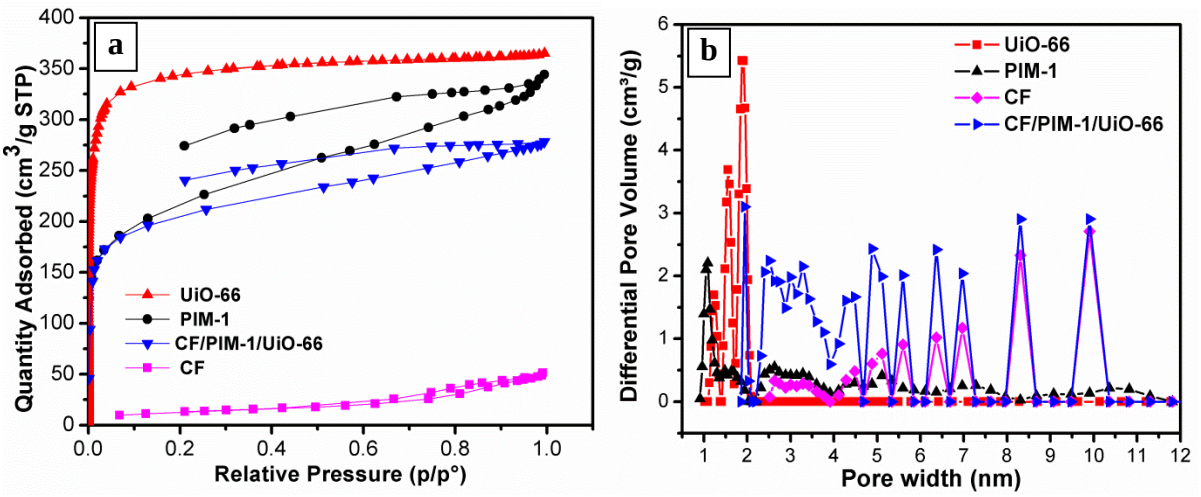

Fig.4 N_2 adsorption-desorption isotherms of pristine and composites materials at 77 K (**a**) and corresponding DFT pore size distribution of pristine materials and the respective CF/PIM-1/UiO-66(Zr) composite (**b**)

A summary of the textural properties of the pristine and composite samples is presented in **Table 1**. From the results, the CF/PIM-1/UiO-66(Zr) composite sample had a specific surface area of 766 m^2g^{-1} which was about 16 times larger than that of the CF (47 m^2g^{-1}). The surface area of the pristine materials (UiO-66(Zr); 1367 m^2g^{-1} and PIM-1; 784 m^2g^{-1}) was found to be notably higher than that of the resulting composite. The observed reduction of surface area of the composite could be ascribed to the insufficient infiltration of the PIM-1 and MOF into the CF macropores. Bearing in mind that the loading wt% of MOF is less when compared to the

combined mass of PIM-1 and CF, this could also explain the decrease of surface area of the resulting composite material. Furthermore, the nitrogen sorption isotherm and pore size distribution curves (**Figure 6.4(a-b)**) of the composite sample displayed a hierarchical porous characteristic which correlates with the morphology of the composite shown in the SEM image (**Fig.3d**).

Table 1 Summary of textural properties and H_2 sorption capacities of pristine and composite materials

Sample	**Measured BET SSA ($m^2 g^{-1}$)[a]**	**Micropore area ($m^2 g^{-1}$)[b]**	**Pore size (nm)[c]**	**Total Pore vol. ($cm^3 g^{-1}$)[d]**	**Measured H_2 uptake (wt. %)[e]**
CF	47	6.58	5.1 – 9.9	0.08	0.04
PIM-1	784	687	1.1 – 10.4	0.53	1.02
UiO-66(Zr)	1367	1303	1.3 – 1.9	0.60	1.38
CF/PIM-1/UiO-66(Zr)	768	645	1.9 – 9.9	0.43	1.05

[a] BET surface area estimated from the N_2 sorption data at 77 K, [b] From t-plot, [c] Pore size determined by DFT analysis, [d] Total pore volume determined from H-K analysis estimated at $p/p^\circ \sim 0.99$, [e] Hydrogen adsorbed at 77 K and 1 bar.

From **Fig.5** the H_2 uptake capacities of PIM-1 (1.02 wt.%) and CF/PIM-1/UiO-66(Zr) (1.05 wt.%) were found to be almost similar. From the comparison of textural properties presented in **Table 1**, the surface areas were found to correlate well with the H_2 uptake capacities. This is in agreement with Chahine's rule **[35]** which states that for every 500 m^2g^{-1} of surface area there is 1 wt.% H_2 adsorption. Nonetheless, our results have shown that anchoring high loadings of PIM-1/UiO-66(Zr) on CF can potentially result in the improved surface area and comparable H_2 uptake if more MOF infiltration into CF is achieved. In this case, the overall properties (textural and H_2 uptake) of the composite were reasonably compromised between the individual pristine counterparts (see **Table 1**). Notably, the H_2 adsorption isotherms of the pristine and composite materials exhibited a steep increase at low pressure up to 1 bar and did not attain adsorption saturation (plateau). Therefore, more H_2 uptake would be expected at higher pressures above 1 bar **[36, 37]**.

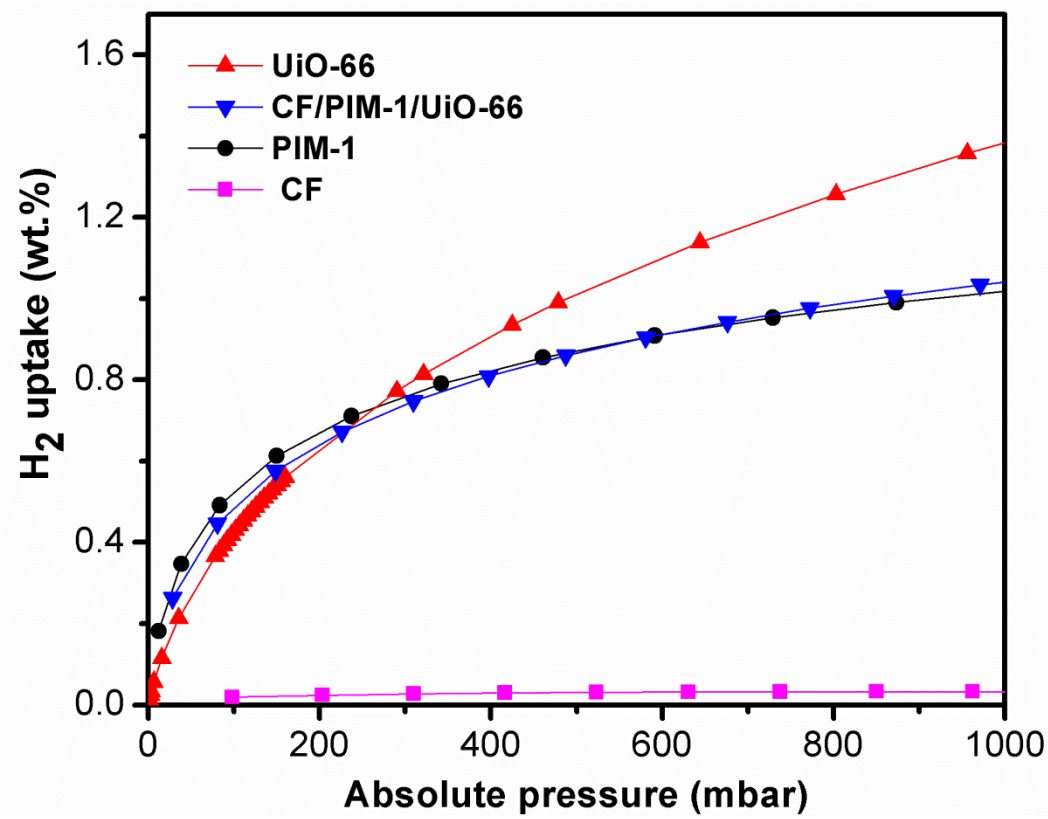

Fig.5 H_2 adsorption isotherms of pristine and composites materials at 77 K and 1 bar

Table 2 presents thermal conductivities of pristine UiO-66(Zr) and PIM-1 as 0.2915 $Wm^{-1}K^{-1}$ and 0.0759 $Wm^{-1}K^{-1}$, respectively at 24 °C. The obtained thermal conductivity value for UiO-66(Zr) is reasonably consistent with the recently reported values for UiO-67 (0.19 $Wm^{-1}K^{-1}$), UiO-66 (0.11 $Wm^{-1}K^{-1}$) and Cu-BTC (0.39 $Wm^{-1}K^{-1}$) which were measured using a transient hot-wire method with 30% uncertainty **[38]**. Although the value obtained in this work for UiO-66 is slightly higher than the one reported in the literature, this may be attributed to the sample preparation method. Differences in sample compaction density were previously reported to impact thermal conductivity values. For example, increasing the pellet density from 0.3 to 0.7 $g.cm^{-3}$ increased the thermal conductivity of compacted MOF-5 from 0.07 to 0.14 $Wm^{-1}K^{-1}$ **[39, 40]**. The thermal conductivities of the pristine carbon foam and CF/PIM-1/UiO-66(Zr) were 0.0703 and 0.1189 $Wm^{-1}K^{-1}$, respectively, when tested under the same conditions (as seen in **Table 1**). The thermal conductivity of CF was found to be comparable with that of the activated carbon-based CF (prepared by thermo-foaming of dispersions of activated carbon powder in an aqueous sucrose resin) reported in the literature (i.e. 0.036–0.049 Wm^{-1} K^{-1}) **[41]**. Surprisingly, the inclusion of CF did not enhance the thermal conductivity of MOFs in CF/PIM-1/UiO-66(Zr) composite, as was initially hypothesised. According to the analytical relations of effective thermal conductivity for highly porous solids, comparison of predictions

by Ashby **[42]** for open cellular structures to those by Maxwell-Eucken **[43]** or Hashin-Shtrikman **[44]**, these findings confirmed that open cells are more insulating than closed cells. Hence, we observed a low thermal conductivity for an open cell CF structure. These results indicate that CF does not have the potential to improve the thermal conductivity of MOFs for managing thermal effects during the H_2 charging and discharging processes due to the large volume insulating pore framework (large spherical pores with thin walls). Therefore, in this case a high pore volume fraction and low densities of the CF and CF/PIM-1/UiO-66(Zr) were limiting factors towards improving the thermal conductivity of the UiO-66(Zr) MOF powder. Future studies should perhaps employ the use of as a conductive polymer such as polyaniline with some modifications **[45].**

Table 2. The three related thermal properties (thermal conductivity, thermal diffusivity and specific heat) of pristine UiO-66(Zr), CF and PIM-1 and hybrid material.

Sample	**Thermal conductivity ($Wm^{-1}K^{-1}$)**	**Thermal diffusivity (mm^2/s)**	**Specific heat (MJ/m^3K)**
CF	0.0703	0.4705	0.1528
PIM-1	0.0759	0.0904	0.8391
UiO-66(Zr)	0.2915	0.8797	0.3314
CF/PIM-1/UiO-66(Zr)	0.1189	0.1662	0.7166

4. Conclusion

Immobilisation of MOF onto an inexpensive carbon foam substrate in the presence of a PIM-1 binding agent was attempted with the expectation of fabricating conductive, lightweight and cost-effective H_2 storage composites materials. The textural properties and hydrogen storage properties of the pristine and composite materials were assessed and compared. The carbon foam-immobilised PIM-1/UiO-66(Zr) composite material exhibited a hydrogen adsorption capacity of 1.05 wt.% at 77 K and pressure up to 1 bar. Thus, the intrinsic H_2 sorption properties of a MOF were retained. Unfortunately, the results have shown that the activated carbon-based foam used in this study is not conductive due to the high void volume. Contrary to our expectations, the incorporation of PIM-1/UiO-66(Zr) into CF only offered better handling but did not lead to the enhancement of thermal conductivity properties. In this case, the actual thermal conductivity of CF/PIM-1/UiO-66(Zr) composite (0.1189 $Wm^{-1}K^{-1}$) was found to be less than that of UiO-66(Zr) MOF (0.2915 $Wm^{-1}K^{-1}$). Future-work will include interrogating

various loadings of PIM-1/UiO-66(Zr) and other conductive adsorbent to obtain higher BET surface areas, enhanced H_2 uptake capacity and better thermal conductivity.

Acknowledgements

The authors acknowledge financial support from the Department of Science and Innovation (DSI) of South Africa towards HySA Infrastructure (Grant No. CNMH01X), National Research Foundation (NRF) for SA/France collaboration funding (Grant No. CNMH20X) and the Royal Society – DFID Africa Capacity Building Initiative Programme Grant (Grant No. AQ150029).

Conflict of interest: The authors declare that they have no conflict of interest.

References

1. K. Cousins, R. Zhang, Polymers. **11**, 690 (2019)
2. U.S. Department of Energy, DOE Technical Targets for On-board Hydrogen Storage for Light-Duty Vehicles. https://www.energy.gov/eere/fuelcells/doe-technical-targets-onboard-hydrogen-storage-light-duty-vehicles. Accessed 19 July 2018
3. K.S. Sing, Pure Appl. Chem. **57**, 603 (1985)
4. Y. He, S. Hwang, D.A. Cullen, M.A. Uddin, L. Langhorst, B. Li, S. Karakalos, A.J. Kropf, E.C. Wegener, J. Sokolowski, M. Chen, Energy Environ. Sci. **12**, 250, (2019)
5. W. Fan, X. Wang, B. Xu, Y. Wang, D. Liu, M. Zhang, Y. Shang, F. Dai, L. Zhang, D. Sun, J. Mater. Chem. A. **6**, 24486, (2018)
6. M. Mozafari, R. Abedini, A. Rahimpour, J. Mater. Chem. A. **6**,12380, (2018)
7. H. Furukawa, N. Ko, Y.B. Go, N. Aratani, S.B. Choi, E. Choi, A.Ö. Yazaydin, R.Q. Snurr, M. O'Keeffe, J. Kim, O.M. Yaghi, Science, **329**, 424, (2010)
8. O.K. Farha, A.Ö. Yazaydın, I. Eryazici, C.D. Malliakas, B.G. Hauser, M.G. Kanatzidis, S.T. Nguyen, R.Q. Snurr, J.T. Hupp, Nat. Chem. **2**, 944, (2010)
9. A.G. Klechikov, G. Mercier, P. Merino, S. Blanco, C. Merino, A.V. Talyzin, Microporous Mesoporous Mater. **210**, 46, (2015)
10. A. Ariharan, B. Viswanathan, V. Nandhakumar, Int. J. Hydrogen Energy. **43**, 5077, (2018)
11. Z. Yang, Y. Xia, R. Mokaya, J. Am. Chem. Soc. **129**, 1673, (2007)
12. Y. Cheng, S. Zhou, P. Hu, G. Zhao, Y. Li, X. Zhang, W. Han, Sci. Rep. **7**, 1439, (2017)

13. N.M. Musyoka, J. Ren, H.W. Langmi, B.C. North, M. Mathe, D. Bessarabov, J. Alloys Compd. **724**, 450, (2017)
14. S.J. Yang, J.Y. Choi, H.K. Chae, J.H. Cho, K.S. Nahm, C.R. Park, Chem. Mater. **21**,1893, (2009)
15. N.M. Musyoka, J. Ren, P. Annamalai, H.W. Langmi, B.C. North, M. Mathe, D. Bessarabov, Res. Chem. Intermed. **42**, 5299, (2016)
16. L.M. Li, F. Yang, H.F. Wang, X.P. Yan, J. Chromatogr. A. **1316**, 97, (2013)
17. L.Y. Molefe, N.M. Musyoka, J. Ren, H.W. Langmi, P.G. Ndungu, R. Dawson, M. Mathe, J. Mater. Sci. **54**, 7078, (2019)
18. M. Inagaki, J. Qiu, Q. G uo, Carbon. **87**, 128, (2015)
19. N. Xiao, Y. Zhou, Z. Ling, Z. Zhao, J. Qiu, Carbon. **60**, 514, (2013)
20. G.M. Psofogiannakis, T.A. Steriotis, A.B Bourlinos E.P. Kouvelos, C. Gch, A.K. Stubos, G.E. Froudakis, Nano. **3**, 933, (2011)
21. C.Y. Zhao, Z.G. Wu, Sol. Energy Mater. Sol. Cells. **95**, 636, (2011)
22. M.L. Pinto, S. Dias, J. Pires, ACS Appl. Mater. Interfaces. **5**, 2360, (2013)
23. J. Ren, T. Segakweng, H.W. Langmi, B.C. North, M. Mathe, J. Alloys Compd. **645**, 170, (2015)
24. P.M. Budd, E.S. Elabas, B.S Ghanem., S. Makhseed, N.B. McKeown, K.J. Msayib, C.E. Tattershall D. Wang, Adv. Mater. **16**, 456, (2004)
25. X. Dyosiba, J. Ren, N.M. Musyoka, H.W. Langmi, M. Mathe, M.S. Onyango, SM&T. **10**, 10, (2016)
26. J. Ren, H.W. Langmi, B.C. North, M. Mathe, D. Bessarabov, Int. J. Hydrogen Energy. **39**, 890, (2014)
27. J.F. Blandez, A. Santiago-Portillo, S. Navalón, M. Giménez-Marqués, M. Álvaro, P. Horcajada, H. García, J. Mol. Catal. A: Chem. **425**, 332, (2016)
28. H.A. Le, S. Chin, J. Jurng, Powder Technol. **225**, 167, (2012)
29. S. Hashemian, K. Salari, Z.A. Yazdi, J. Ind. Eng. Chem. **20**, 1892, (2014)
30. L. Giraldo, J.C. Moreno-Pirajan, Orient. J. Chem. **30**, 451, (2014)
31. H.A. Zakaria, W.S.W. Mansor, N. Shahrin, Int. J. Sci. Technol. **3**, 502, (2017)
32. P. Hester, S. Xu, W. Liang, N. Al-Janabi, R.,Vakili, P. Hill, C.A. Muryn, X. Chen, P.A. Martin, X. Fan, J. Catal. **340**, 85, (2016)
33. Q. Yang, H.Y. Zhang, L. Wang, Y. Zhang, J. Zhao, ACS Omega. **3**, 4199, (2018)
34. Z. Li, K. Wang, J. Song, Q. Xu, N. Kobayashi, J. Mater. Cycles Waste. **16**, 359, (2014)
35. B.Panella, M. Hischer, S. Roth, Carbon. 43,2209.

36. J. Ren, N.M. Musyoka, H.W. Langmi, B.C. North, M. Mathe, X. Kang, Int. J. Hydrogen Energy. **39**, 14912, (2014).
37. Y. Sun, L. Wang, W. A. Amer, H. Yu, J. Ji, L. Huang, J. Shan, R. Tong, J. Inorg. Organomet. Polym. Mater. 23, 270–285 (2013).
38. J. Huang, X. Xia, X. Hu, S. Li, K. Liu, Int. J. Heat Mass Transf. **138**, 11, (2019)
39. S.T. Meek, J.A. Greathouse, M.D. Allendorf, Adv. Mater. **23**, 249, (2011)
40. J.J. Purewal, D. Liu, J. Yang, A. Sudik, D.J. Siegel, S. Maurer, U. Müller, Int. J. Hydrogen Energy. **37**, 2723, (2012)
41. R. Narasimman, S. Vijayan, K. Prabhakaran, J. Mater. Res. **30**, 46, (2015)
42. M.F. Ashby, Phil. Phil. Trans. R. Soc. A. **364**, 15, (2005)
43. J.C. Maxwell, A treatise on electricity and magnetism, Vol. (Oxford: Clarendon Press, 1873).
44. Z. Hashin, S. Shtrikman, J. Appl. Phys. **33**, 3125, (1962)
45. Z. Neisi, Z. Ansari-Asl, A.S. Dezfuli, J. Inorg. Organomet. Polym. Mater. 29, 1838–1847 (2019)